# Visible-light photocatalysis in CdTe nanoflakes with exposed {111} facets and charge separation between polar CdTe {111}surfaces

Guoping Han [a,b], Weina Wang [c], Bin Liu [a], Cuijin Pei [a], Hua Zhao [a], Junfang Liu [a], Heqing Yang [a,*]

[a] Shaanxi Key Laboratory for Advanced Energy Devices, Shaanxi Engineering Laboratory for Advanced Energy Technology, Key Laboratory of Macromolecular Science of Shaanxi Province, School of Materials Science and Engineering, Shaanxi Normal University, Xi'an, 710119, China
[b] School of Science, Xi'an University of Architecture and Technology, Xi'an, 710055, China
[c] Key Laboratory of Macromolecular Science of Shaanxi Province, School of Chemistry and Chemical Engineering, Shaanxi Normal University, Xi'an 710119, China

## ARTICLE INFO

## ABSTRACT

The search for active semiconductor photocatalysts that can utilize adequately solar-energy remains to be an open issue. CdTe nanoflakes and nanowires with a range of texture coefficients of (111) have been synthesized. Photocatalytic activities of the CdTe nanocrystals in degradation of malachite green, methyl orange, acid red 88 and ciprofloxacin can be enhanced by increasing the texture coefficients of (111) and reducing texture coefficient of (220). The exposed polar {111} facets were found to be the active facets, and a charge separation model between polar Cd-CdTe (111) and Te-CdTe ($\bar{1}\,\bar{1}\,\bar{1}$) surfaces is proposed. An internal electric field is created between polar Cd-CdTe (111) and Te-CdTe ($\bar{1}\,\bar{1}\,\bar{1}$) surfaces by the spontaneous polarization, and the internal electric field drives separation of the photoinduced electrons and holes. Therefore, the CdTe nanoflakes with exposed polar {111} facets synthesized by using oleylamine as a morphology controlling agent show superior photocatalytic activity, compared with CdTe nanowires, nanocrystals with irregular shapes and commercial powders as well as CdS branched nanostructures. The charge separation model provides a clear opinion into charge transfer in the semiconductor nanocrystals with exposed active facets, and affords guidance to design more effective photocatalysts, solar cells and other photoelectronic devices.

© 2017 Elsevier B.V. All rights reserved.

## 1. Introduction

The physical and chemical properties of semiconductor nanocrystals are not only sensitive to crystal size and shape but also to crystal facets. Thus, shape and facet-controlled synthesis of semiconductor nanocrystals have attracted significant research activities [1–3]. Cadmium telluride (CdTe), an important p-type II−VI compound semiconductor with a direct band gap of 1.44 eV and a high optical absorption coefficient in the visible spectrum, is considered as a great candidate material for photovoltaics [4,5]. Nanoparticals [6], nanorods [7], nanowires [8], nanoribbons [9], nanotetrapods [10], nanoplatelets [11], nanorod/nanowire arrays [12,13] and 3D-ordered porous nanocrystals [14] of CdTe have been synthesized by various chemical methods until now. A Field-effect transistor was fabricated using single CdTe nanowire [15]. The CdTe nanoribbons, nanoplatelets, nanorod arrays and nanowires were employed to fabricate photodetectors [9,11,12] and nanogenerator [16]. In addition, multisegment CdTe−Au−CdTe nanowire sensors for the detection of DNA molecules have been developed [17]. However, very little is known about the facet effects of CdTe nanocrystals on their physical and chemical properties.

The key issue in photocatalysis is to develop photocatalysts with high catalytic activities. Since the discovery of photoinduced decomposition of water on TiO$_2$ electrodes [18], thousands of kinds of photocatalysts have been developed [19–23]. However, the search for active semiconductor photocatalysts that can utilize adequately solar-energy remains to be an open issue. Regarding optical absorption, CdTe is an excellent solar light harvester due to its band gap matching the preferred range of the solar irradiation spectrum [4]. It has been used to sensitize ZnO [24] and TiO$_2$ [25] as a visible light absorber to obtain highly efficient photocatalysts.
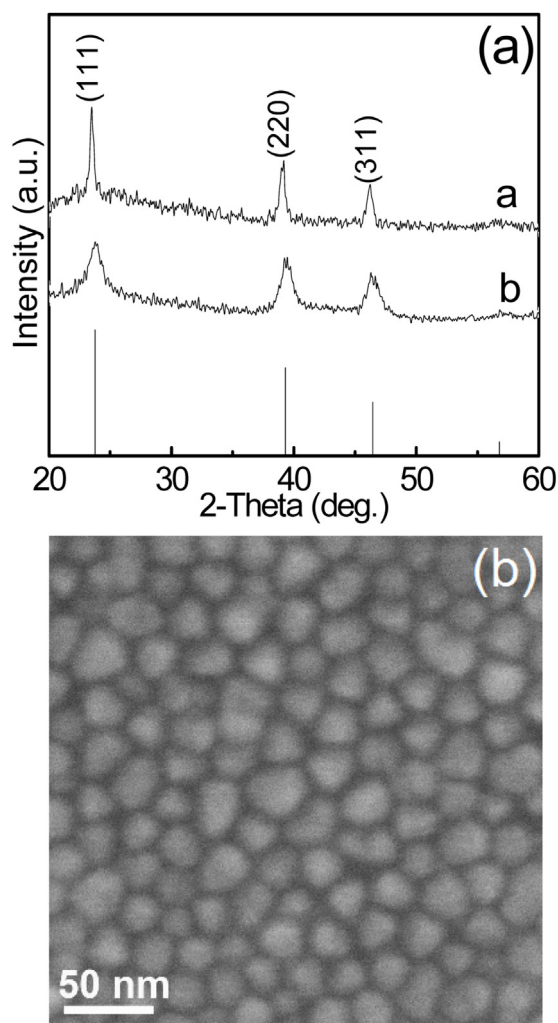
**Fig. 1.** (a) XRD patterns of the-as synthesized CdTe products at 300 (a) and 200 °C (b). The stick pattern is the standard XRD pattern of cubic CdTe powders with Cu Kα radiation (JPCDS card no. 65–1085). (b) SEM image of the as-synthesized CdTe products at 300 °C.

However, the investigation on study of photocatalytic behavior of pure CdTe semiconductor is very rare [26].

Recently, the exposing polar facet of semiconductor photocatalysts has been found to be an effective strategy to increase photocatalytic activity [27–30]. Herein, we report on the controllable synthesis of CdTe nanocrystals with a range of (111) texture coefficients and the (111) texture coefficient-dependent photocatalytic activity in degradation of organic dyes and antibiotics. The CdTe {111} facets were proven to be the active facets. The active {111} facets were found to be polar surfaces by periodic density functional theory (DFT) calculations. Based on the polar structure, a charge separation model between polar Cd-CdTe (111) and Te-CdTe ($\bar{1}\,\bar{1}\,\bar{1}$) surfaces was proposed to explain the enhanced photocatalytic activities.

## 2. Experimental section

### 2.1. Preparation

All reagents and solvents were used as received without further purification in our experiments.

#### 2.1.1. CdTe nanoflakes

In a typical synthesis, 0.0128 g (0.1 mmol) of Te powder and 1.0 mL of tri-$n$-octylphosphine (TOP) (90%) were added into a 50 mL of three-neck flask, heated at 220 °C for 1 h under stirring and an $O_2$-free $N_2$ atmosphere to form a clear yellowish Te-TOP solution. In a separate three-neck flask, 22.80 mg (0.1 mmol) of $CdCl_2$·2.5$H_2O$ was added in 5.0 mL of oleylamine (OLA) (90%), and heated in a sand bath under nitrogen and active stirring to form a transparent Cd-OLA solution. when the sand bath temperature reaches 300 or 200 °C, the Te-TOP solution was injected quickly into the hot Cd-OLA solution, and the temperature was kept at 300 or 200 °C for 30 min. Subsequently, the flask was cooled to room temperature. 5.0 mL of chloroform and 15.0 mL methanol were added in the resultant solution to yield a brown black precipitate. The products were separated by centrifuging, washed three times with absolute ethanol. Finally, the products were dried under vacuum for further characterization.

#### 2.1.2. CdTe nanowires

In a typical procedure, 24 mL of ethylene glycol (EG), 1 mL of ethylenediamine (en), 0.0617 g (0.2 mmol) of $Cd(NO_3)_2$·4$H_2O$ and 0.0443 g (0.2 mmol) of $Na_2TeO_3$ were added in order into a 50 mL of Teflon-lined autoclave. The mixture was stirred for 1.0 h to form a clear solution. The autoclave was sealed and heated at 180 °C for 24 h. After the heating treatment, the autoclave was cooled to room temperature. The product was collected by centrifugation, washed three times with deionized water and absolute ethanol, respectively. Finally, the products were dried under vacuum and stored in vacuum desiccators.

### 2.2. Characterization

The morphology and dimension of the as-obtained products were observed on a scanning electron microscope (SEM) (FEI Quanta 200) at an accelerating voltage of 20 kV, a SU8000 field emission scanning electron microscope at an accelerating voltage of 30 kV and a transmission electron microscope (TEM) (JEOL JEM-3010) at an accelerating voltage of 300 kV. The samples for TEM were fabricated by dispersing the as-obtained CdTe nanocrystals on a carbon-coated copper grid. The XRD patterns were obtained on a Rigaku D/MAX-IIIC X-ray diffractometer with Cu Kα1 radiation (λ = 1.541 Å) at 40 kV and 30 mA. Each specimen was scanned at a step size of 0.02° and a scanning speed of 2°/min with diffraction angles varying between 20 and 60°. The infrared (IR) spectrum was recorded using a Bruker Equinx 55 fourier transform IR spectrophotometer. The Brunauer-Emmett-Teller (BET) specific surface area determination was performed by nitrogen adsorption/desorption using an America Micromeritics ASAP 2020 surface analytical instrument. Ultraviolet-visible (UV-vis) diffuse reflectance spectra were obtained on a Perkin Elmer Lambd 950 spectrophotometer. XPS spectra were recorded by using a Kratos Axisultra X-ray photoelectron spectrometer with an excitation source of $Al_{K\alpha}$ = 1486.7 eV. The binding energies obtained in the XPS analysis were corrected for specimen charging by referencing C 1s to 284.6 eV.

### 2.3. Evaluation of photocatalytic activity

The three kinds of organic dyes, malachite green (MG), methyl orange (MO) and acid red 88 (AR 88) and a kind of antibiotics, ciprofloxacin (CIP) were selected as model molecules to examine the photocatalytic activity of the CdTe nanocrystals. Molecule structures of these dyes and antibiotics are shown in Fig. S1 in the supporting information. 10.0 mg of the as-prepared CdTe nanocrystals or commercial CdTe powders were added to 10.0 mL of $5.0 \times 10^{-5}$ M MG/MO solution, $2.5 \times 10^{-4}$ M AR 88 or $1.8 \times 10^{-5}$ M
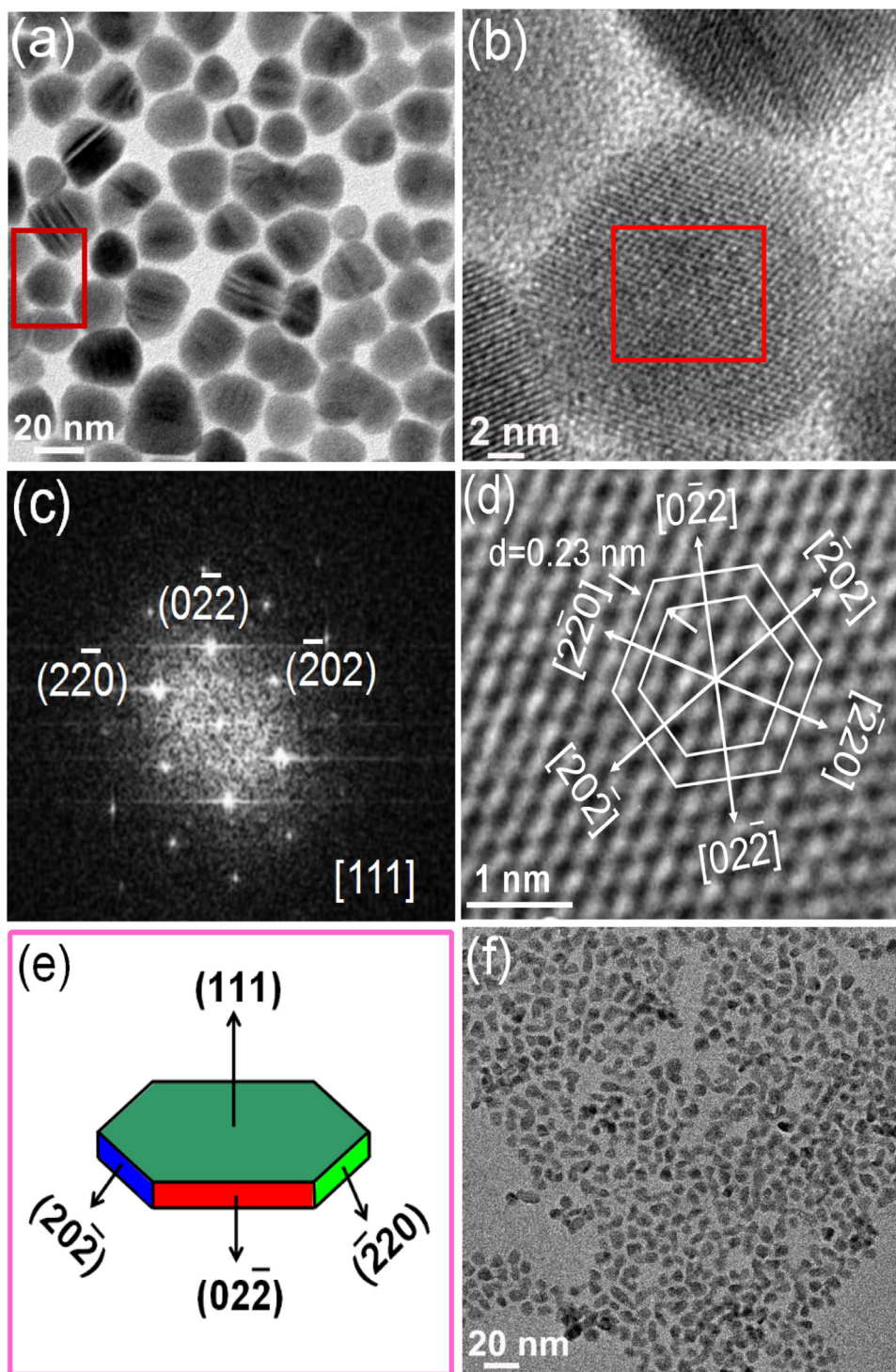
**Fig. 2.** (a) and (b) TEM images of the products synthesized at 300 °C. (c) and (d) FFT pattern and HRTEM image from box in (b). (e) The crystal orientation of the CdTe nanoflakes. (f) TEM image of the products synthesized at 200 °C.

CIP solution to get a suspension. The suspension was stirred for 20, 30, 20 or 40 min in the dark. The mixed solution was then irradiated by a 500 W Xe lamp which is equipped with an optical filter (≥420 nm) to cut off the light in the ultraviolet region. At a given irradiation time interval, 3 mL of sample was withdrawn from the test tube for analysis. Sample solution was obtained by centrifugation, and its absorption spectrum was measured on a Hitachi U-2910 spectrophotometer using deionized water as a reference.

## 3. Results and discussion

### 3.1. Morphology and crystal structure of CdTe nanocrystals

The products synthesized in the CdCl$_2$-OLA-Te-TOP reaction system at 200 and 300 °C were characterized with XRD and TEM. Fig. 1(a) shows the XRD patterns of the CdTe nanocrystals synthesized at 200 and 300 °C. The XRD patterns confirm that these CdTe nanocrystals have cubic structures by giving characteristic (111),
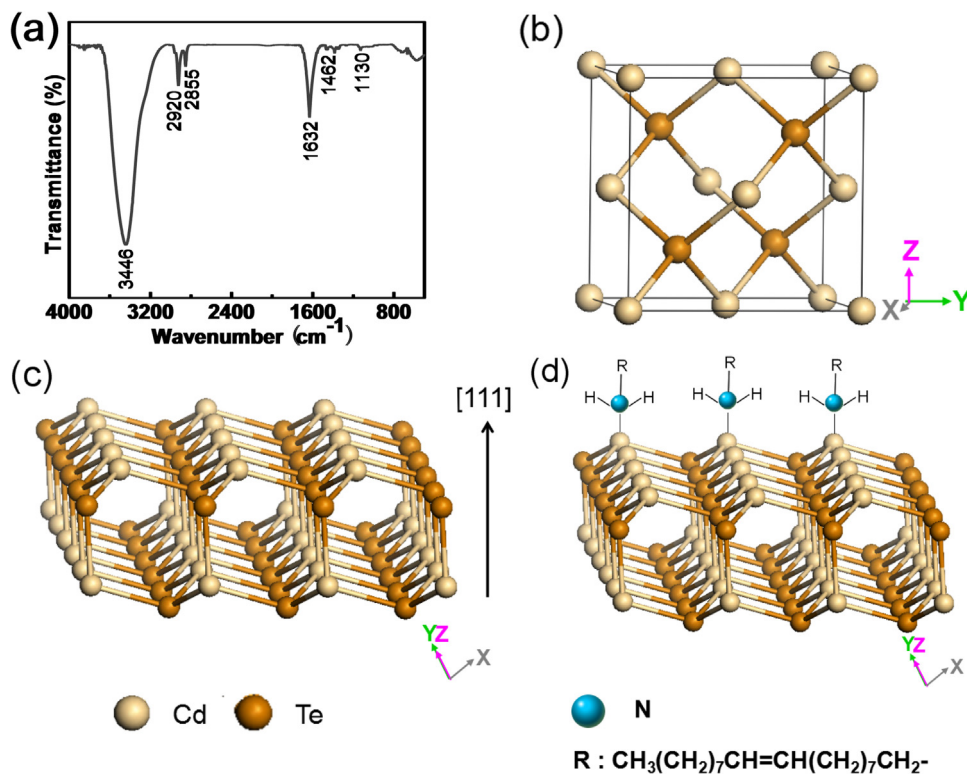
**Fig. 3.** (a) IR spectrum of the as-prepared CdTe nanoflakes. (b) The crystal structure of cubic phase CdTe. (c) The atomic structures of (111) surface obtained from periodic DFT calculations. (d) The OLA molecules adsorbed selectively on the (111) surface.

(220), and (311) peaks. Moreover, the (111) intensity increases with an increase on the reaction temperature, indicating (111) orientation is enhanced. The texture coefficient of (111) plane (TC(111)) is defined as [31]:
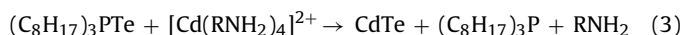
$$TC(111) = \frac{I(111)}{I_0(111)} \left\{ \frac{1}{n} \sum \frac{I(hkl)}{I_0(hkl)} \right\}^{-1} \qquad (1)$$

Where I(hkl) are measured intensities of (hkl) reflection, $I^0(hkl)$ are powder diffraction intensities of cubic CdTe according to the Joint Committee on Powder Diffraction Standards (JCPDS) card no. 65–1085, and n is the number of diffraction peaks used in the calculations. For materials with random crystallographic orientations, e.g. powders, the texture coefficient is 1. Values of TC(111) for the nanocrystals obtained at 300 and 200 °C are 1.41 and 0.96, respectively. Fig. 1(b) shows SEM image of the-as synthesized CdTe products at 300 °C for 30 min. The SEM observation reveals that the products obtained at 300 °C consist of CdTe nanoparticles with the sizes of 14.8–22.6 nm. Fig. 2(a) shows a representative TEM images of the samples obtained at 300 °C. It is obvious that the geometrical shape of the CdTe nanoparticles is a flake. The typical sizes of the nanoflakes are in the range of 14.0–24.4 nm, which corresponds with the SEM observation. Fig. 2(b) presents an enlargement of the boxed region in (a), which indicates that the surfaces of the nanoflakes are clean, and without any sheathed amorphous phase. Fig. 2(c) and (d) show the fast Fourier transform (FFT) pattern and high resolution TEM (HRTEM) image from box in (b), respectively. The FFT and HRTEM show that the nanoflakes are single crystalline, grow along six symmetric directions of $< \bar{2}02 >$ and are enclosed by (111) top and $(\bar{1}\,\bar{1}\,\bar{1})$ bottom surfaces. The crystal orientation schematic illustration of the CdTe nanoflakes is shown in Fig. 2(e). When reaction temperature was decreased to 200 °C, the as-synthesized products consist of nanocrystals with irregular shapes (Fig. 2(f)), the size range of nanocrystals is 6.7–9.6 nm.

### 3.2. Formation mechanism of the CdTe nanoflakes

In order to understand the growth mechanism, the IR spectrum of the as-obtained nanoflakes at 300 °C was measured, and the result is shown in Fig. 3(a). In the IR spectrum, the band at 3446 cm$^{-1}$ attributed to asymmetrical stretching vibration of NH$_2$ of OLA [32] and the asymmetrical and symmetrical stretching vibration bands of the −CH$_2$ (2920 and 2855 cm$^{-1}$) [33] were observed. Moreover, the stretching vibration band of the C=C (1632 cm$^{-1}$), CH$_2$ bending vibration (1460 cm$^{-1}$) and −C−N stretching mode (1070 cm$^{-1}$) were also found. The IR spectrum suggests that oleylamine molecules are adsorbed on the surface of the CdTe nanoflakes.

In the reaction system, Cd$^{2+}$ reacted firstly with OLA (RNH$_2$, R: CH$_3$(CH$_2$)$_7$CH=CH(CH$_2$)$_7$CH$_2$-) to form [Cd(RNH$_2$)$_4$]$^{2+}$. When the reaction temperature is at 200 or 300 °C, the [Cd(RNH$_2$)$_4$]$^{2+}$ reacted with (C$_8$H$_{17}$)$_3$PTe to form CdTe. The chemical reactions are formulated as follows [34]:

$$Cd^{2+} + RNH_2 \rightarrow [Cd(RNH_2)_4]^{2+} \qquad (2)$$

$$(C_8H_{17})_3PTe + [Cd(RNH_2)_4]^{2+} \rightarrow CdTe + (C_8H_{17})_3P + RNH_2 \qquad (3)$$

The crystal structure of cubic phase CdTe is displayed in Fig. 3(b). The Cd atom is tetrahedrally coordinated to four Te atoms. The Te atoms are coordinated to four Cd atoms in a cube. The atomic structure of (111) surface was investigated by periodic DFT calculations [35], and the result is given in Fig. 3(c). As shown in Fig. 3(c), the (111) surface termination consists of a layer of unsaturated Cd sites, and Cd atoms on the (111) plane are three-coordinated Cd. In the reaction system, the OLA molecules may serve as ligands to Cd, and adsorbs selectively on the Cd-CdTe (111) surface (Fig. 3(d)). The presence of OLA impedes the growth of (111) surface, and thus CdTe nanoflakes grow along the $< \bar{2}02 >$ directions, leading to form CdTe nanoflakes with exposed (111) and $(\bar{1}\,\bar{1}\,\bar{1})$ facets.
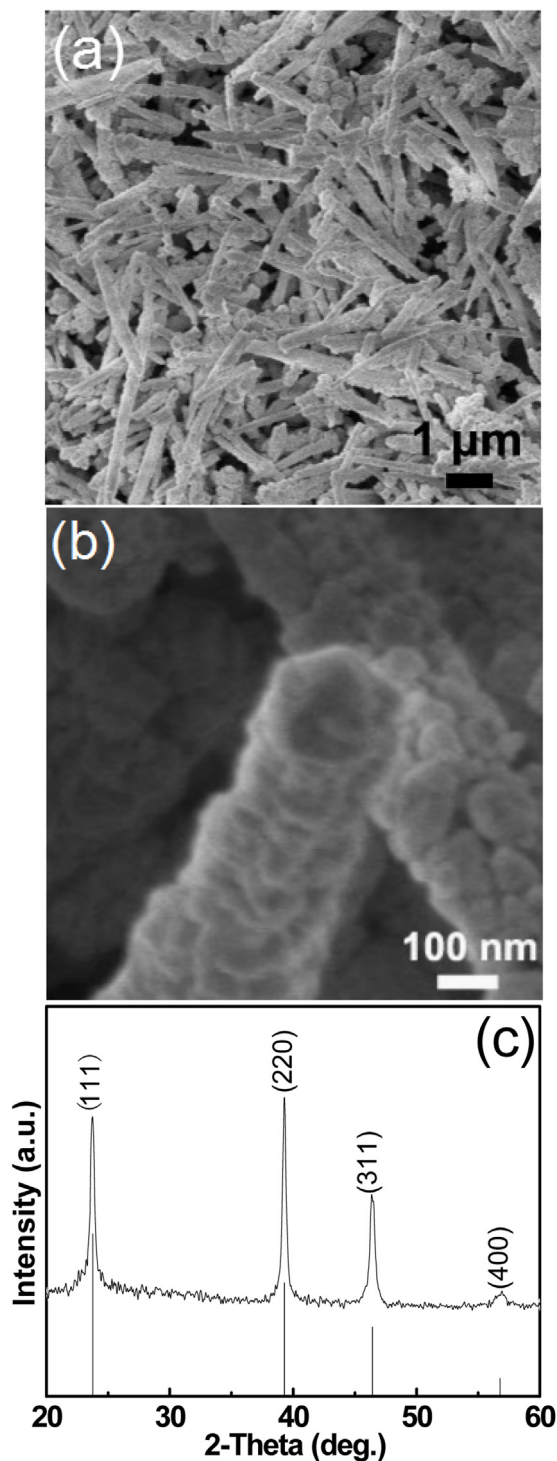
**Fig. 4.** (a)–(b) SEM images and (c) XRD pattern of the as-synthesized CdTe nanowires.

### 3.3. Morphology and crystal structure of CdTe nanowires

Fig. 4(a) and (b) exhibit typical SEM images of the as-synthesized CdTe nanowires. The lengths and diameters of the CdTe nanowires are in the range of 2.2–4.5 μm and 90–230 nm, respectively. The nanowire in Fig. 4(b) has a hexagonal cross section with a side length of about 90 nm and a diagonal of about 210 nm. XRD pattern from the nanowires in Fig. 4(c) indicates that the sample is cubic structured CdTe. TEM image reveals that the geometrical shape of the CdTe nanostructures is a cone (Fig. S2(a)). The diameter of the
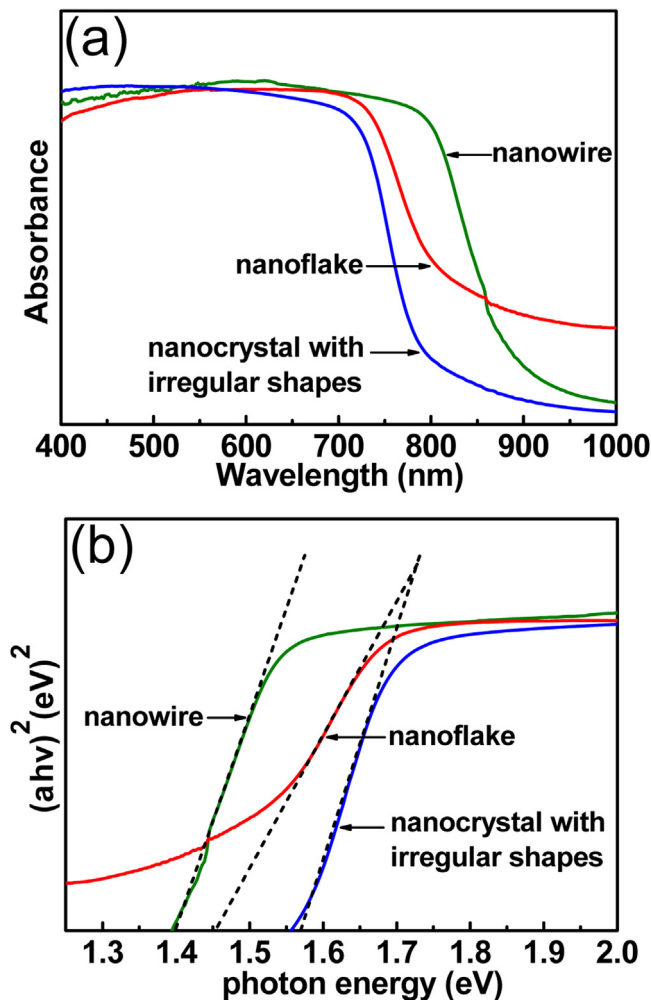


**Fig. 5.** (a) The diffuse reflectance spectra and (b) the plot of $(\alpha h\nu)^2$ versus photon energy ($h\nu$) for the CdTe nanoflakes, nanocrystals with irregular shapes and nanowires.

nanowires on the tip is about 125 nm. The selected area electron diffraction (SAED) pattern from box in (a) is shown in Fig. S2(b), which can be indexed as the [011] zone axis of CdTe with the cubic structure. The corresponding HRTEM image is shown in Fig. S2(c). The (111) atomic planes with a lattice distance of 0.37 nm can be observed clearly from the HRTEM image. The SAED and HRTEM results indicate that the CdTe nanowires grow along [111] direction. The schematic illustration of crystal orientation of the CdTe nanowires is shown in Fig. S2(d).

### 3.4. UV–vis diffuse reflectance spectra

The diffuse reflectance spectra of CdTe nanowires, nanoflakes and nanocrystals with irregular shapes are shown in Fig. 5, which reveal that CdTe nanostructures have good optical absorption property in the visible spectrum. For CdTe with a direct band gap, the optical absorption near the band edge follows the formula [36],

$$\alpha h\nu = A(h\nu - E_r)^{1/2} \tag{4}$$

Where $\alpha$, $\nu$, $E_r$ and $A$ are the absorption coefficient, light frequency, band gap energy, and a constant, respectively. The band gap energy ($E_r$ value) of the as-obtained CdTe nanocrystals can be thus estimated from a plot of $(\alpha h\nu)^2$ versus photon energy ($h\nu$). For the nanowires, nanoflakes and nanocrystals with irregular shapes, the result is measured to be about 1.40, 1.46 and 1.57 eV, respectively.

The changes in the $E_r$ can be explained due to quantum confinement effect of carrier. For a spherical ultrafine particles of radius r, the lowest excitation band gap $E_r$ can be expressed as [37,38]

$$E_r \cong E_g + \frac{\hbar^2 \pi^2}{2r^2}\left(\frac{1}{m_e} + \frac{1}{m_h}\right) \tag{5}$$

where $E_g$ is the band gap for bulk crystal, $m_e$ and $m_h$ are the effective masses of the electron and hole, respectively, $\hbar$ is Planck's constant divided by $2\pi$. When nanoparticle size is decreased the lowest excitation band gap $E_r$ increases. Figs. 2 and 4 indicate that size of the nanowires is larger than that of the nanoflakes and the nanocrystals with irregular shapes, and size of the nanocrystals with irregular shapes is the smallest. $E_r$ value of the nanocrystals with irregular shapes and the least size is thus the largest (1.57 eV), and the nanowires have the least $E_r$ of 1.40 eV.

## 3.5. Photocatalytic activity

To demonstrate the potential applicability in photocatalysis of the as-obtained CdTe nanoflakes, we investigated their photocatalytic activity using degradation of MG, MO, AR 88 and CIP as references, and compared with that of CdTe nanowires, nanocrystals with irregular shapes and commercial powders. The SEM image and XRD pattern from the CdTe commercial powders are shown in Fig. S3, which indicate that the samples are composed of cubic CdTe particles with irregular geometrical morphologies.

Before test of the photocatalytic activity, adsorption kinetics of the as-obtained CdTe nanoflakes, nanocrystals with irregular shapes, nanowires and commercial powders for MG, MO, AR 88 and CIP were studied, and the results are shown in Fig. S4(a)–(d). It was found that for MG, after 20 min value of $C/C_0$ over CdTe nanoflakes, nanocrystals with irregular shapes, nanowires and commercial powders is 0.70, 0.69, 0.72 and 0.88, respectively, and hardly decreased with increasing the time, which reveal that an adsorption/desorption equilibrium between MG and the four kinds CdTe catalysts is achieved within 20 min. For MO, AR 88 and CIP, the adsorption/desorption equilibrium is achieved within 30, 20 and 40 min, respectively. The suspension containing the dye and the CdTe catalysts was thus stirred for 20, 30, 20 and 40 min for MG, MO, AR 88 and CIP, respectively, in the dark before the Xe lamp irradiation.

The temporal absorption spectra of MG, MO, AR 88 and CIP solution during the photocatalytic degradation over the CdTe nanoflakes under visible light irradiation ($\lambda \geq 420$ nm) are shown in Fig. S5(a)–(d). MG, MO, AR 88 and CIP show a maximum absorption band at 616, 462, 502 and 276 nm, respectively. The four absorption peaks diminished gradually over the CdTe nanoflakes as the irradiation time was extended. After visible light irradiation 21 min for MG, 175 min for MO, 128 min for AR 88 and 400 min for CIP, their absorption intensity is reduced by about 89.5, 84.4, 94.7 and 73.7%, respectively, which imply that the MG, MO, AR 88 and CIP molecules may be decomposed. The results indicate that the as-synthesized CdTe nanoflake is an effective photocatalyst.

Fig. 6(a)–(d) shows the photocatalytic degradation of MG, MO, AR 88 and CIP in solutions without catalyst and over CdTe commercial powders, nanowires, nanocrystals with irregular shapes and nanoflakes, respectively. It can be clearly seen that the decomposition of MG, MO, AR 88 and CIP progress relaxedly in absence of catalyst. However, the MG, MO, AR 88 and CIP decomposition over the CdTe catalysts fleetly progress, and MG, MO, AR 88 and CIP decomposition rates over the CdTe nanoflakes are faster than that over CdTe nanocrystals with irregular shapes, nanowires and commercial powders. Fig. 7(a)–(d) shows the fittings of $\ln C_0/C$ plot versus time over the CdTe nanoflakes, nanocrystals with irregular shapes, nanowires and commercial powders for MG, MO, AR 88 and CIP, respectively. The photodegradation of MG, MO, AR 88 and CIP catalyzed by the four kinds of CdTe catalysts fits pseudo first-order reaction. i.e. $\ln C_0/C = kt$, k is the apparent rate constant of the degradation. In our experiment, the measured k values were listed in Table 1. Apparently, the CdTe nanoflakes show higher photocatalytic activities than CdTe nanocrystals with irregular shapes, nanowires and commercial powders.

The BET surface area of the CdTe nanoflakes, nanocrystals with irregular shapes, nanowires and commercial powders was measured, and the result is 16.9, 17.0, 13.3 and 7.5 m$^2$g$^{-1}$, respectively. The MG, MO, AR 88 and CIP degradation apparent rate constants per unit surface area of the four kinds of CdTe catalysts, as for the basis for the comparison, were examined in this work. It is found that whether degradations of MG, MO, AR 88 or CIP, the normalized rate constant values ($k'$) for the CdTe nanoflakes is much higher than that for CdTe nanocrystals with irregular shapes, nanowires and commercial powders, as shown in Fig. 8 and Table 1. The results clearly demonstrate that the CdTe nanoflakes have superior intrinsic photocatalytic activity, compared with CdTe nanocrystals with irregular shapes, nanowires and commercial powders. According to Figs. 2 and S2, the exposed facets of the CdTe nanoflakes and nanowires are {111} and {220} facets. The percentage of {111} facets of the CdTe nanoflakes is higher than that of the nanowires, and percentage of {220} facets is lower than that of the nanowires. In addition, TC(111) of nanowires and commercial powders was computed to be 0.89 and 0.79, respectively (Table 1 and Fig. 8). Moreover, The texture coefficient of (220) plane (TC(220)) is defined as [31]:

$$TC(220) = \frac{I(220)}{I_0(220)} \left\{ \frac{1}{n} \sum \frac{I(hkl)}{I_0(hkl)} \right\}^{-1} \tag{6}$$

TC(220) for four kinds of CdTe photocatalysts is completed, and the result is shown in Table 1 and Fig. 8. It was found that photocatalytic activity of CdTe can be enhanced by an increase on the TC(111) and a decrease on the TC(220). It is thus reasonable to conclude that the exposed {111} facets are highly reactive facets, and the {220} facets are not.

In addition, according to the method of Jin et al. [39], the branched CdS nanostructures were synthesized. The as-prepared products were characterized by SEM and XRD, and the results were presented in Fig. S6. As can be seen that the as-products consisted of wurtzite CdS branched nanostructures. We investigated photocatalytic activities of branched CdS nanostructures in degradation of MG, MO, AR 88 and CIP, and compared with that of the CdTe nanoflakes. Fig. S7 shows adsorption kinetics of the CdS branched nanostructures for MG, MO, AR 88 and CIP, which indicates that the adsorption/desorption equilibrium is achieved within 20, 40, 20 and 40 min, for MG, MO, AR 88 and CIP, respectively. Fig. S8(a)–(d) shows the photocatalytic degradation of MG, MO, AR 88 and CIP in solutions over the CdS branched nanostructures and CdTe nanoflakes, respectively. It is clear that the CdTe nanoflakes exhibit higher photocatalytic activities than branched CdS nanostructures for degradation of MG, MO, AR 88 and CIP.

## 3.6. Charge separation between polar CdTe (111) and ($\overline{111}$) surfaces

Surface energy of the exposed CdTe (111) and (220) facets was calculated using DFT [40,41], it is found that CdTe (111) facet has higher surface energy, 1.63, comparing to 1.48 for (110) facet. Structure of the CdTe (110) surface was investigated by periodic DFT calculations, and the result is shown in Fig. 9(a). The (110) face is nonpolar surface, which is terminated with Cd and Te atoms, as shown in Fig. 9(a). However, the {111} facets are polar surfaces, they include a positive (111) plane terminated with Cd atoms, and
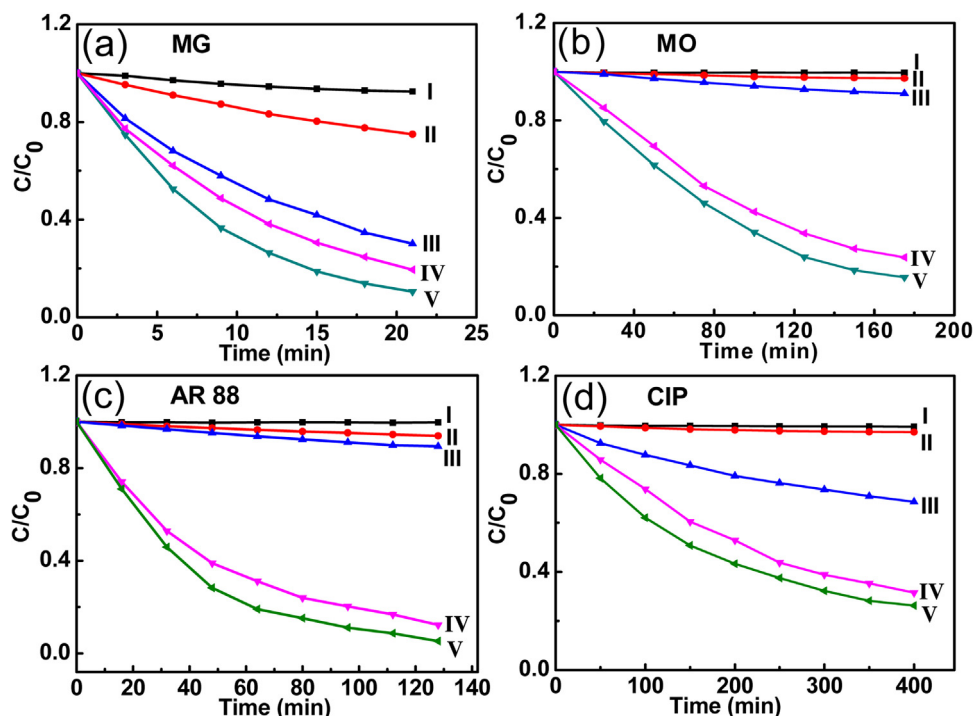
**Fig. 6.** (a)–(d) Photocatalytic degradation of the MG (a), MO (b), AR 88 (c) and CIP (d) solutions without catalyst (I), over CdTe commercial powders (II), nanowires (III), nanocrystals with irregular shapes (IV) and nanoflakes (V) under Xe light irradiation ($\lambda \geq 420\,nm$).
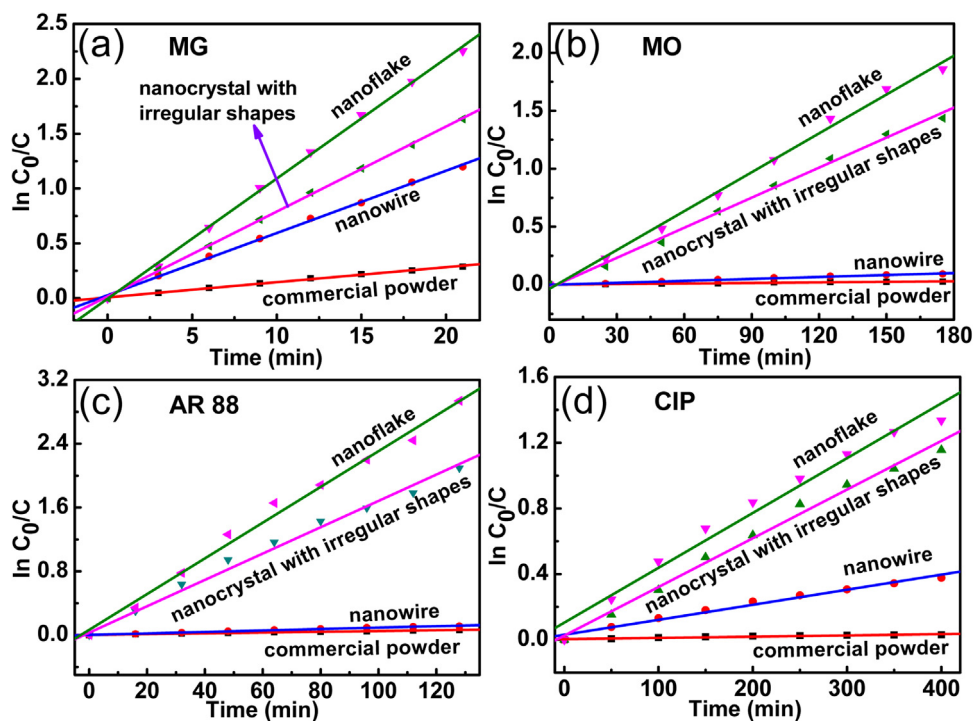


**Fig. 7.** (a)–(d) The fitting of $lnC_0/C$ plot vs. time over CdTe nanoflakes, nanocrystals with irregular shapes, nanowires and commercial powders for MG (a), MO (b), AR 88 (c) and CIP (d) solutions.

a negative ($\bar{1}\,\bar{1}\,\bar{1}$) plane terminated with Te atoms, as shown in Fig. 3(c).

The atomic charge distribution in the [111] direction obtained from periodic DFT calculations [42] is shown in Fig. 9(b). Apparently, each layer contains all positive $Cd^{2+}$ ions or all negative $Te^{2-}$ ions in the [111] direction. Cd atomic charge on the Cd-CdTe (111)

plane is +0.228 and Te atomic charge on the Te-CdTe ($\bar{1}\,\bar{1}\,\bar{1}$) plane is −0.304. The charge-centers of cations and anions separate and result in an electric dipole. An internal electric field thus is generated between the positive Cd-CdTe (111) and negative Te-CdTe ($\bar{1}\,\bar{1}$ $\bar{1}$) planes due to the spontaneous polarization. A charge separation

**Table 1**
TC(111), TC(220), BET surface area, k and $k'$ of the CdTe nanoflakes, nanocrystals with irregular shapes, nanowires and commercial powders.

| Sample | | nanoflake | nanocrystal with irregular shapes | nanowire | commercial powder |
|---|---|---|---|---|---|
| TC(111) | | 1.41 | 0.96 | 0.89 | 0.79 |
| TC(220) | | 1.01 | 1.12 | 1.37 | 1.68 |
| BET($m^2 g^{-1}$) | | 16.9 | 17.0 | 13.3 | 7.5 |
| k($min^{-1}$) | MG solution | 0.10954 ±0.00151 | 0.07744 ±0.00063 | 0.05673 ±0.00096 | 0.01374 ±0.00037 |
| | MO solution | 0.01117 ±0.00031 | 0.00863 ±0.00023 | 0.00056 ±0.00002 | 0.00016 ±0.00001 |
| | AR 88 solution | 0.0224 ±0.00080 | 0.01651 ±0.00027 | 0.00091 ±0.00003 | 0.00049 ±0.00001 |
| | CIP solution | 0.00334 ±0.00018 | 0.00296 ±0.00010 | 0.00092 ±0.00004 | 0.000076 ±0.000008 |
| $ki$($min^{-1} m^{-2}$) | MG solution | 0.6481 | 0.4555 | 0.4265 | 0.1832 |
| | MO solution | 0.0661 | 0.0508 | 0.0042 | 0.0021 |
| | AR 88 solution | 0.1325 | 0.0971 | 0.0068 | 0.0065 |
| | CIP solution | 0.0198 | 0.0174 | 0.0069 | 0.0010 |

k: The MG, MO, AR 88 and CIP degradation apparent rate constants,$k'$: The MG, MO, AR 88 and CIP degradation apparent rate constants per unit surface area.
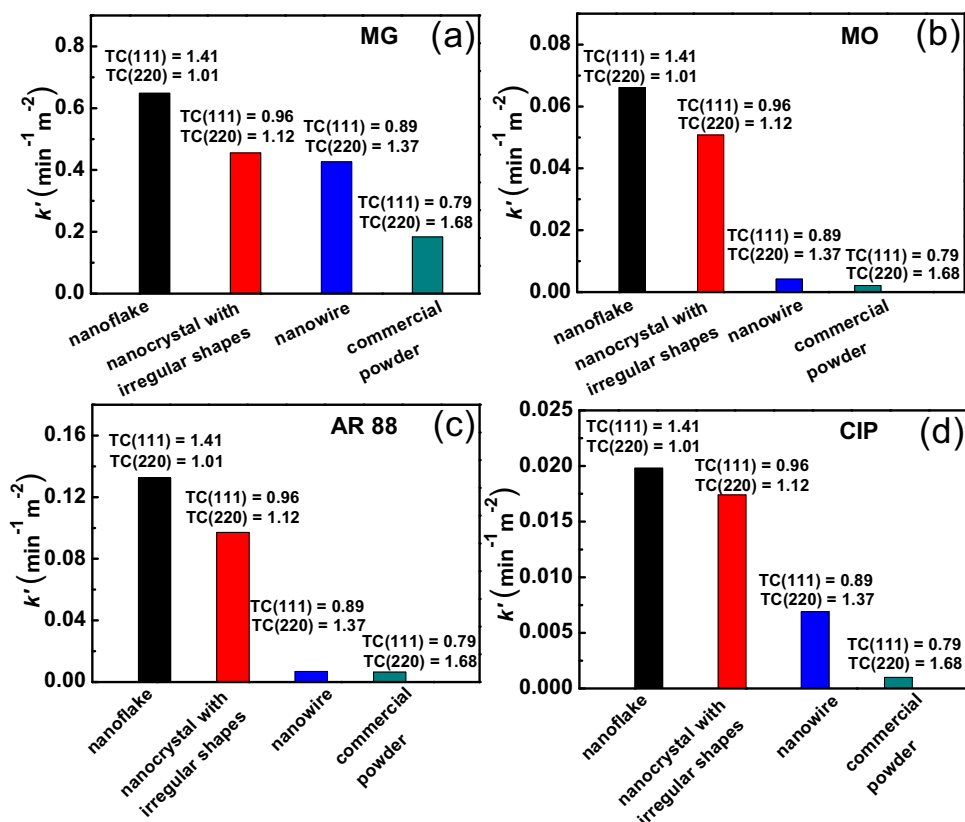


**Fig. 8.** Normalized apparent rate constants ($ki$) of MG (a), MO (b), AR 88 (c) and CIP (d) degradation per unit surface area over CdTe nanoflakes, nanocrystals with irregular shapes, nanowire and commercial powders.

model between polar Cd-CdTe (111) and Te-CdTe ($\bar{1}\,\bar{1}\,\bar{1}$) surfaces is thus proposed to explain the enhanced photocatalytic activities.

As the CdTe nanoflakes with exposed Cd-CdTe (111) and Te-CdTe ($\bar{1}\,\bar{1}\,\bar{1}$) polar surfaces were used as photocatalysts, the visible light irradiation induces a transition of electrons from the valence-band to the conduction-band, leaving an equal number of vacant sites (holes), and thus electron-hole pairs were formed in the CdTe nanoflakes (Fig. 9(c)). The photoinduced electrons and holes migrate to the positive polar Cd-CdTe (111) surface and the nega-tive polar Te-CdTe ($\bar{1}\,\bar{1}\,\bar{1}$) surface, respectively, under the internal

electric field (Fig. 9(d)). The oxidation and reduction reactions take place on the Te-CdTe ($\bar{1}\,\bar{1}\,\bar{1}$) surface and the Cd-CdTe (111) surface, respectively (Fig. 9(d)). The good charge separation between Cd-CdTe (111) and Te-CdTe ($\bar{1}\,\bar{1}\,\bar{1}$) polar surfaces can effectively reduce the probability of recombination of photogenerated charges, the exposed CdTe {111} facets are thus photocatalytic active facets. When the TC(111) value of CdTe nanocrystals increases, the per-centage of the exposed {111} facets increases, and thus superior photocatalytic activity was observed in CdTe nanoflakes with high TC(111) value.
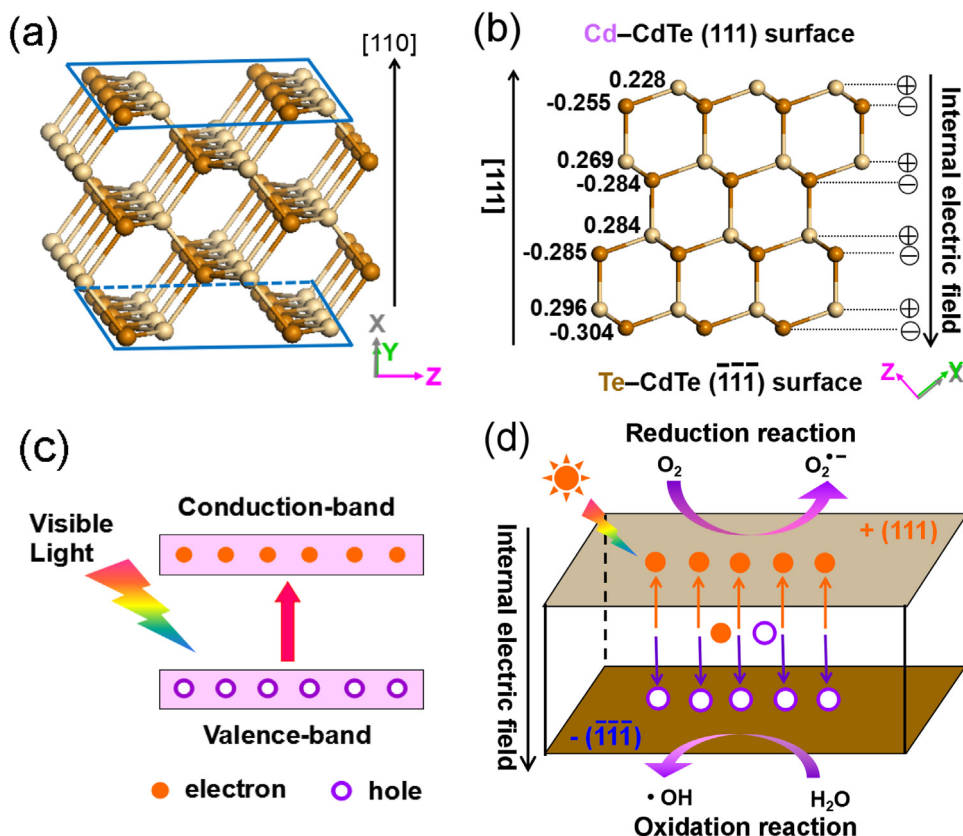
**Fig. 9.** (a) The atomic structures of (110) surface obtained from periodic DFT calculations. (b) The atomic charge distribution in the [111] direction obtained from periodic DFT calculations. (c) Generation of electron-hole pairs in the CdTe nanoflakes. (d) The schematic illustration of charge separation between Cd-CdTe (111) and Te-CdTe ($\bar{1}\,\bar{1}\,\bar{1}$) polar surfaces and photocatalytic reactions.
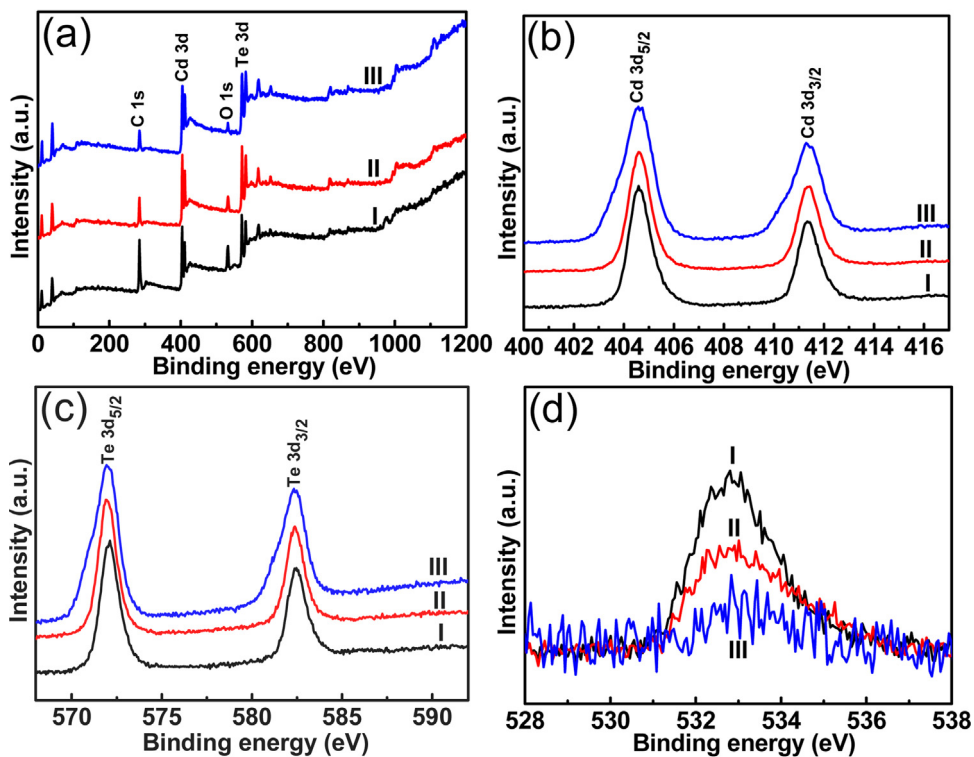


**Fig. 10.** XPS spectra, including (a) the survey spectrum, (b) Cd $3d_{5/2}$ and $3d_{3/2}$, (c) Te $3d_{5/2}$ and $3d_{3/2}$, (d) O 1s of CdTe nanoflakes (I), nanocrystals with irregular shapes (II) and nanowires (III).

Moreover, the surface states of the three kinds of CdTe nanocrystals were investigated using X-ray photoelectron spectroscopy. The results are shown in Fig. 10, including (a) the survey spectra, (b) Cd $3d_{5/2}$ and $3d_{3/2}$, (c) Te $3d_{5/2}$ and $3d_{3/2}$ and (d)O 1s spectra. The binding energy of Cd $3d_{5/2}$ and Cd $3d_{3/2}$ was identified at 404.6 and 411.4 eV, respectively [43]. In the case of Te, $3d_{5/2}$ and $3d_{3/2}$ peaks were observed at 571.9 and 582.3 eV, respectively [43,44]. The O 1s peak centered at about 532.8 eV corresponds chemisorbed oxygen species [45].The presence of the O 1s peak in XPS indicates that molecular oxygen ($O_2$) are adsorbed at the surface of CdTe nanocrystals, and the change of adsorption oxygen ability follows the order of CdTe nanoflakes > nanocrystal with irregular shapes > nanowires. The (111) surface of CdTe nanoflakes is terminated with the unsaturated Cd atoms with dangling bonds. The unsaturated Cd atoms can adsorb oxygen molecules due to the deficiency of Te and positive electricity in air. The adsorbed oxygen molecules can capture free electrons in CdTe nanoflakes and may play an important role in photocatalysis. The adsorbed oxygen molecules are conducive to the elimination of the photoinduced electrons and the separation of photoproduced charges because of strong attracting electron ability, the oxidation reaction is thus enhanced on the Te-CdTe ($\bar{1}\,\bar{1}\,\bar{1}$) surface. Therefore, photocatalytic activity of CdTe nanocrystals in degradation of organic pollutants can be enhanced by increasing adsorption oxygen ability, and thus CdTe nanoflakes with exposed {111} facets show superior photocatalytic activity in comparison with CdTe nanocrystals with irregular shapes and nanowires.

## 4. Conclusions

In summary, CdTe nanocrystals with a range of (111) texture coefficients have been successfully synthesized. The photocatalytic activity of CdTe nanocrystals in degradation of MG, MO AR 88 and CIP is enhanced by increasing the TC(111), and the {111} facets were proved to be the active facets. Based on polar structure of the exposed {111} surfaces, a charge separation model between polar (111) and ($\bar{1}\,\bar{1}\,\bar{1}$) surfaces was proposed to explain the enhanced photocatalytic activities. The charge separation model not only explains the enhanced photocatalytic performance of semiconductor photocatalyst active facets, but also provides new insights into the design and fabrication of advanced photocatalytic materials, solar cells and other photoelectronic devices.

## Acknowledgements

## Appendix A. Supplementary data

Supplementary data associated with this article can be found, in the online version, at http://dx.doi.org/10.1016/j.apcatb.2017.02.054.

## References

[1] K. Zhou, Y.D. Li, Angew. Chem. Int. Ed. 51 (2012) 602–613.
[2] Z.Y. Jiang, Q. Kuang, Z.X. Xie, L.S. Zheng, Adv. Funct. Mater. 20 (2010) 3634–3645.
[3] H. Tong, S.X. Ouyang, Y.P. Bi, N. Umezawa, M. Oshikiri, J.H. Ye, Adv. Mater. 24 (2012) 229–251.
[4] M.C. Kum, H. Jung, N. Chartuprayoon, W. Chen, A. Mulchandani, N.V. Myung, J. Phys. Chem. C 116 (2012) 9202–9208.
[5] F. Jiang, J.J. Liu, Y.C. Li, L.Z. Fan, Y.Q. Ding, Y.F. Li, Adv. Funct. Mater. 22 (2012) 2402–2411.
[6] H.B. Shen, H.Z. Wang, X. Chen, J.Z. Niu, W.W. Xu, X.M. Li, X.D. Jiang, Z.L. Du, L.S. Li, Chem. Mater. 22 (2010) 4756–4761.
[7] X.P. Jin, J. Li, J. Parisi, J.K. Olesiak, J. Nanopart. Res. 13 (2011) 6963–6970.
[8] J.W. Sun, L.W. Wang, W.E. Buhro, J. Am. Chem. Soc. 130 (2008) 7997–8005.
[9] X. Xie, S.Y. Kwok, Z.Z. Lu, Y.K. Liu, Y.L. Cao, L.B. Luo, J.A. Zapien, I. Bello, C.S. Lee, S.T. Lee, W.J. Zhang, Nanoscale 4 (2012) 2914–2919.
[10] M.D. Goodman, L. Zhao, K.A. DeRocher, J. Wang, S.K. Mallapragada, Z.Q. Lin, ACS Nano 4 (2010) 2043–2050.
[11] S. Pedetti, B. Nadal, E. Lhuillier, B. Mahler, C. Bouet, B. Abeícassis, X.Z. Xu, B. Dubertret, Chem. Mater. 25 (2013) 2455–2462.
[12] X.N. Wang, J. Wang, M.J. Zhou, H.J. Zhu, H. Wang, X.D. Cui, X.D. Xiao, Q. Li, J. Phys. Chem. C 113 (2009) 16951–16953.
[13] E. Matei, L. Ion, S. Antohe, R. Neumann, I. Enculescu, Nanotechnology 21 (2010) 105202–105208.
[14] L.L. Yang, Z.H. Yang, W.X. Cao, L. Chen, J. Xu, H.Z. Zhang, J. Phys. Chem. B 109 (2005) 11501–11504.
[15] W.I. Park, H.S. Kim, S.Y. Jang, J. Park, S.Y. Bae, M. Jung, H. Leec, J. Kimd, J. Mater. Chem. 18 (2008) 875–880.
[16] T.C. Hou, Y. Yang, Z.H. Lin, Y. Ding, C. Park, K.C. Pradel, L.J. Chen, Z.L. Wang, Nano Energy 2 (2013) 387–393.
[17] X. Wang, C.S. Ozkan, Nano Lett. 8 (2008) 398–404.
[18] A. Fujishima, K. Honda, Nature 238 (1972) 37–38.
[19] D.T. Zhou, Z. Chen, Q. Yang, C. Shen, G. Tang, S.L. Zhao, J.J. Zhang, D. Chen, Q.H. Wei, X.P. Dong, ChemCatChem 8 (2016) 3064–3073.
[20] S.L. Chen, A.J. Wang, C.T. Hu, C. Dai, J.B. Benziger, AIChE J. 58 (2012) 568–572.
[21] G. Zhang, Z.Y. Hu, M. Sun, Y. Liu, L.M. Liu, H.J. Liu, C.P. Huang, J.H. Qu, J.H. Li, Adv. Funct. Mater. 25 (2015) 3726–3734.
[22] A.B. Djurisic, Y.H. Leung, A.M.C. Ng, Mater. Horiz. 1 (2014) 400–410.
[23] J.H. Yang, D. Wang, H.X. Han, C. Li, Acc. Chem. Res. 46 (2013) 1900–1909.
[24] C. Eley, T. Li, F.L. Liao, S.M. Fairclough, J.M. Smith, G. Smith, S.C.E. Tsang, Angew. Chem. Int. Ed. 53 (2014) 7838–7842.
[25] Y.S. Li, F.L. Jiang, Q. Xiao, R. Li, K. Li, M.F. Zhang, A.Q. Zhang, S.F. Sun, Y. Liu, Appl. Catal. B 101 (2010) 118–129.
[26] M.A. Golsefidi, M.F. Ramandi, M.A.K. Shahkooie, J. Mater. Sci. Mater. Electron. http://dx.doi.org/10.1007/s10854-016-5360-1.
[27] Y. Chen, H. Zhao, B. Liu, H.Q. Yang, Appl. Catal. B 163 (2015) 189–197.
[28] B. Liu, H.Q. Yang, A.H. Wei, H. Zhao, L.C. Ning, C.J. Zhang, S.Z. Liu, Appl. Catal. B 172–173 (2015) 165–173.
[29] B. Liu, L. Ma, L.C. Ning, C.J. Zhang, G.P. Han, C.J. Pei, H. Zhao, S.Z. Liu, H.Q. Yang, Appl. Mater. Interfaces 7 (2015) 6109–6117.
[30] B. Liu, L.C. Ning, H. Zhao, C.J. Zhang, H.Q. Yang, S.Z. Liu, Phys. Chem. Chem. Phys. 17 (2015) 13280–13289.
[31] H. Zhao, W.Y. Yin, M.Y. Zhao, Y.Z. Song, H.Q. Yang, Appl. Catal. B 130–131 (2013) 178–186.
[32] J.L. Zhang, R.S. Srivastava, R.D.K. Misra, Langmuir 23 (2007) 6342–6351.
[33] W.B. Bu, Z.X. Chen, F. Chen, J.L. Shi, J. Phys. Chem. C 113 (2009) 12176–12185.
[34] G.P. Han, L. Wang, C.J. Pei, R.Y. Shi, B. Liu, H. Zhao, H.Q. Yang, S.Z. Liu, J. Alloys Compd. 610 (2014) 62–68.
[35] B. Delley, J. Chem. Phys. 92 (1990) 508–517.
[36] Q. Liang, H. Zhao, L.C. Ning, J.L. Wang, C.J. Zhang, L. Wang, A.H. Wei, Q. Zhao, H.Q. Yang, S.Z. Liu, Appl. Catal. B 152–153 (2014) 390–396.
[37] L. Brus, J. Phys. Chem. 90 (1986) 2555–2560.
[38] H.Q. Yang, B.L. Zhang, X.G. Wang, X.J. Wang, T. Li, S.H. Xie, X. Yao, J. Cryst. Growth 280 (2005) 521–529.
[39] R. Jin, M.Y. Su, J. Wang, P. Zhang, M. Cui, Y. Chen, H.Q. Yang, Mater. Res. Bull. 47 (2012) 3070–3077.
[40] J.P. Perdew, K. Burke, M. Ernzerhof, Phys. Rev. Lett. 77 (1996) 3865–3868.
[41] M.D. Segall, P.J.D. Lindan, M.J. Probert, C.J. Pickard, P.J. Hasnip, S.J. Clark, M.C. Payne, J. Phys.: Condens. Matter. 14 (2002) 2717–2744.
[42] F.L. Hirshfeld, Theor. Claim. Acta 44 (1977) 129–138.
[43] H. Zhang, Z. Zhou, B. Yang, J. Phys. Chem. B 107 (2003) 8–13.
[44] S.S. Garje, J.S. Ritch, D.J. Eisler, M. Afzaal, P. O'Brien, T. Chivers, J. Mater. Chem. 16 (2006) 966–969.
[45] X.F. Wang, J.J. Xu, H.Y. Chen, J. Phys. Chem. C 112 (2008) 7151–7157.